Calculating the interior permanent-magnet motor

T.J.E. Miller, M. Popescu, C. Cossar, M. McGilp, J.A. Walker

SPEED Laboratory, Glasgow G12 8LT, UK

Abstract - **This paper describes the calculation of torque in a brushless permanent-magnet line-start a.c. motor by means of the flux-MMF diagram in combination with the finite-element method. Results are compared with measured flux-MMF diagrams, with shaft torque measurements, and with torque calculated using the classical phasor diagram.**

I. INTRODUCTION

The interior permanent-magnet motor (IPM) is a hybrid permanent-magnet/reluctance synchronous brushless motor that is being developed for several applications such as servo motors, elevator drive motors, and electric vehicle traction motors, [1-6,10,12]. Line-start IPM motors are also used for compressors and other applications requiring a high-efficiency alternative to the induction motor; these are often capacitor motors fed from a single-phase supply, as is the motor in Fig. 1, [8]. In many cases the windings are not sine-distributed and the current and EMF waveforms may be non-sinusoidal.

Saturation of the magnetic circuit is particularly complex in these motors: different sections of the machine saturate independently, causing large and sometimes time-varying changes in equivalent-circuit parameters such as inductances and EMF. Unfortunately these are the parameters used in classical methods for calculating torque, current, and voltage.

It therefore becomes unclear to what extent it is safe to rely on classical methods based on equivalent circuits and (in the case of sinewave machines) on phasors and *dq*-axis theory.

The finite-element method is capable of calculating the electromagnetic behavior, but it is rather slow, and it has no *a priori* relationship with the classical theory of operation of the machine.

Funding for this work was provided by the companies of the *SPEED* Consortium. J.A. Walker is partially supported by the U.K. Engineering and Physical Sciences Research Council, by the *SPEED* Consortium, and by Robert Bosch GmbH. Test motors were kindly provided by Electrolux Compressors, Italy; see [8].

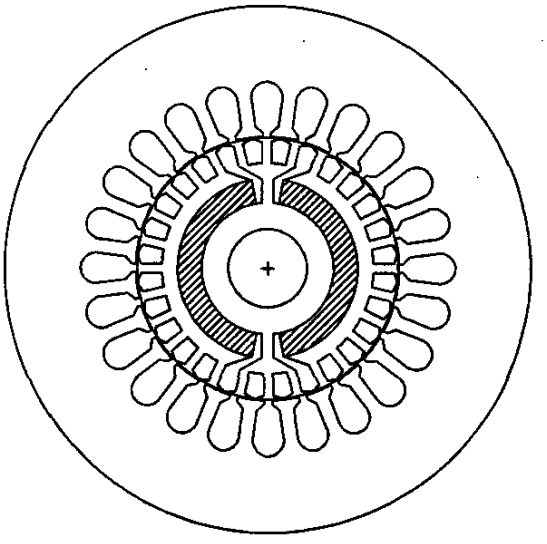

Fig. 1. Cross-section of the 2-pole capacitor motor analyzed. The arc-shaped ferrite magnets are shaded.

This paper shows that for "sinewound" machines, which have sinusoidally distributed stator ampere-conductors, the elliptical flux-MMF diagram [2,11] calculated by classical theory can be readily compared with the same diagram computed by the finite-element method. The comparison provides the link between the finite-element method and the classical theory.

The comparisons throw considerable light on the effect of saturation on the *d*- and *q*-axis parameters, particularly the synchronous reactances X_d and X_q. Because of the difficulty of calculating unambiguous saturated values of X_d and X_q, it is argued that the flux-MMF diagram should be routinely used, especially as its calculation is straightforward using the finite-element method.

The flux-MMF diagram can be measured directly using a digital recording oscilloscope, and the torque calculated from its enclosed area can be compared with the shaft torque obtained from dynamometer tests. These results are presented as experimental validation of the flux-MMF diagram.

0-7803-7817-2/03/$17.00 ©2003 IEEE

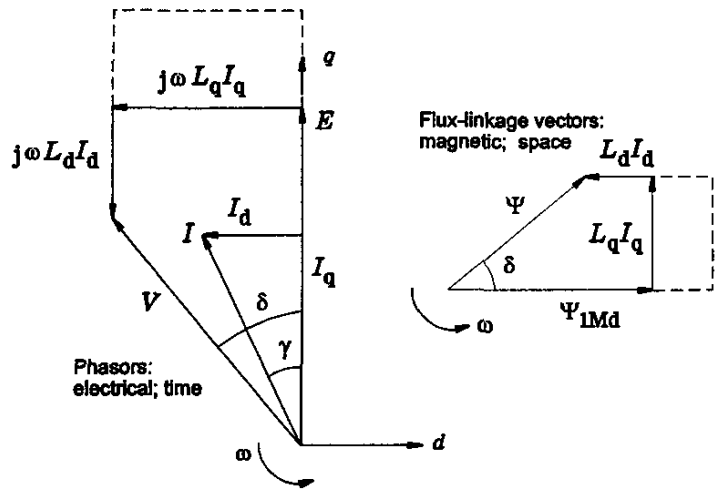

Fig. 2. Phasor diagram and flux-linkage vector diagram. On the left are the electrical quantities, i.e., voltages and currents. On the right are the corresponding magnetic flux-linkages. The dotted lines show the lack of uniqueness in the saturated values of X_d and E. For simplicity, resistance is neglected in this diagram, but normally it must be included.

II. Theory

A. *Phasor Diagram for Sinewave Operation*

The phasor diagram (Fig. 2) is drawn for one phase of a motor operating with balanced sinusoidal currents so that only the positive sequence field exists. It is assumed that the windings produce a sinusoidal distribution of ampere-conductors around the periphery of a smooth cylindrical stator bore (apart from slotting). The EMF and terminal voltage waveforms are also sinusoidal in time.

The phasor diagram is not only useful in understanding how the torque is limited by the voltage and current available from the drive, but it is also the basis of the circle diagram which is useful for understanding the effect of changes in speed and load, [1,2]. The electromagnetic torque T_e is given in terms of the rms current components I_d and I_q and the synchronous reactances X_d and X_q by

$$T_e = \frac{mp}{\omega}[EI_q + I_d I_q (X_d - X_q)]. \quad (1)$$

where m is the number of phases, p is the number of pole-pairs, ω is the radian frequency, and E is the rms fundamental open-circuit EMF per phase. In terms of the fundamental d- and q-axis flux-linkage components Ψ_d and Ψ_q, the equation for T_e can be expressed as

$$T_e = mp(\Psi_d I_q - \Psi_q I_d) \quad (2)$$

B. *Effect of Saturation*

Equations (1) and (2) remain valid for the fundamental components even under saturated conditions. Recognizing this, many engineers try to work with "saturated values of X_d and X_q", [1-8]. However, it is not often stated that the saturated value of X_d is not unique. The equation

$$\Psi_d = \frac{1}{\omega}\left[E + X_d I_d\right] \quad (3)$$

shows that for any value of d-axis current I_d there is an infinite number of pairs of values of E and X_d that will produce the d-axis flux-linkage Ψ_d that is actually present in the winding.

The lack of uniqueness in the saturated values of E and X_d is illustrated in Fig. 2, where the dotted line construction produces the same value of airgap flux (and flux-linkage Ψ) as the solid lines. It means that the actual airgap flux cannot be uniquely apportioned to the magnet and the armature MMF.

Many estimates of the "saturated value" of X_d tacitly assume that E is constant. For example, in finite-element analysis the permeability in every element of the mesh may be "frozen" at the open-circuit value: the additional flux-linkage due to stator current is computed with these permeabilities, and its ratio to the current that is causing it is taken as a measure of the synchronous inductance.

No matter whether the total flux-linkage is used to derive "total inductance", or whether the additional flux-linkage is used to define "incremental inductance", the process of freezing permeabilities is arbitrary, and can lead to confusion as to which value should be used in equations such as (1). Difficulties can arise in the interpretation of the results of this method, such as discontinuities in the graph of X_d vs. I_d when I_d changes from positive to negative; (see Fig. 13).

Equation (2) suggests that apportionment of q-axis voltage (or d-axis flux-linkage) between E and $X_d I_d$ is actually unnecessary, not only for calculating the torque but even for solving the voltage equations of the circuit, which in the steady state are

$$\begin{aligned} V_d &= R_a I_d - j\omega\Psi_q; \\ V_q &= R_a I_q + j\omega\Psi_d. \end{aligned} \tag{4}$$

If V_d and V_q are known, these equations can be solved for I_d and I_q provided that the relationships between I_d and Ψ_d and between I_q and Ψ_q are known. The functions $\Psi_d(I_d)$ and $\Psi_q(I_q)$ are known as the *magnetization curves* in the d and q axes, and they can be pre-computed by the finite-element method without any ambiguity as to how much flux is attributed to the magnet and how much to the current. Where there is significant cross-saturation, the flux-linkages can be made functions of both currents, i.e. $\Psi_d(I_d, I_q)$ and $\Psi_q(I_d, I_q)$.

C. *The Flux-MMF Diagram*

The flux-MMF diagram is the locus of a point whose coordinates are flux and MMF, or more conveniently, flux-*linkage* ψ and current i in each phase of the machine, [11]. Over one cycle the area W enclosed within this locus is equal to the electromechanical energy conversion in that phase. If the induced voltage (i.e., the terminal voltage minus the resistance voltage drop) and the current are both sinusoidal, the flux-MMF diagram is elliptical as shown in Fig. 3(a).

In a brushless motor with squarewave current drive and trapezoidal EMF, the diagram is composed approximately of two parallelograms as in Fig. 3(b).

If the phases are balanced, the average electromagnetic torque is derived from the variation of co-energy with rotor position over one cycle:

$$T_e = m\frac{W}{2\pi}. \tag{5}$$

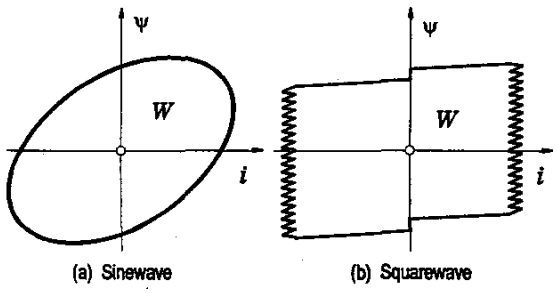

Fig. 3. i-ψ loops for sinewave and squarewave drives

The torque equation (2) is a special case of (5) in which W is the area of the ellipse whose dimensions in the current and flux-linkage axes are defined by I and Ψ respectively. The simplicity of (2) follows from the simple elliptical shape of Fig. 3(a).

The flux-MMF diagram is completely general. It works for *any* waveforms of current and flux-linkage, and does not require sinusoidally distributed windings or sinusoidal time-waveforms of voltage or current. Since the EMF in each phase is equal to $d\psi/dt$, it works for motors having *any* EMF waveform. It also includes cogging torque.

The simple classical form of the torque equation such as (2) arises only under special ideal conditions characterized by the simple geometric shape of the flux-MMF diagram. In the general case these ideal conditions are not met.

D. *Calculation of the Flux-MMF Diagram*

In classical theory the time-waveforms of flux-linkage and current are expressed by (6) with phase angles and amplitudes as in Fig. 2:

$$\begin{aligned} i(\omega t) &= i_1 \cos \omega t \\ \text{and } \psi(\omega t) &= \psi_1 \cos [\omega t + (\delta - \gamma - \pi/2] \end{aligned} \tag{6}$$

where ψ_1 is derived from the phasor diagram using relationships such as (4). Then the flux-MMF diagram follows directly in a plot of ψ vs. i.

In the finite-element method, the waveform $i(\omega t)$ is applied to the conductor distribution at each of a series of rotor positions such as the one shown in Fig. 4. Simultaneously the appropriate current waveforms are applied to the conductors of the other phases. The flux-linkage ψ of each phase is computed from the weighted summation of vector potentials over the respective conductor areas within the stator slots. Then, as in the classical method, the flux-MMF diagram follows directly in a plot of ψ vs. i.

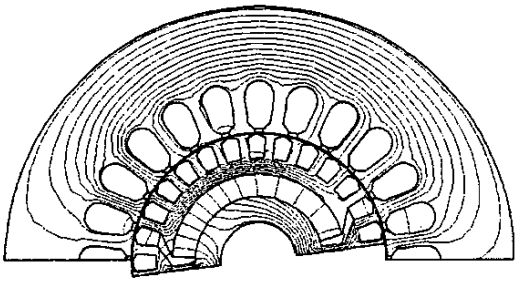

Fig. 4. Finite-element calculation

The flux-MMF diagram obtained in this way includes all flux-linkage components except the end-turn leakage. In particular, slot-leakage is included.

Examples of ψ-i diagrams obtained by both methods are compared with test data in Section III.

E. Extracting E, X_d and X_q from finite-element data

As suggested earlier, the equivalent circuit and the phasor diagram with E, X_d, X_q are not needed for calculating the torque, if the finite-element method is available to be used with the flux-MMF diagram or the Maxwell stress method. However, the finite-element method has no quick means of calculating how much current will flow for a given applied voltage, or *vice-versa*. For this reason it is desirable to correlate the finite-element method with the equivalent-circuit calculation. For sinewave motors it is convenient to do this by extracting values of E, X_d and X_q from the finite-element results.

One way to do this is to use the finite-element method to calculate the self- and mutual inductances of the phase windings directly, as a function of rotor position, since the reactances X_d and X_q can be derived from these. As mentioned earlier, permeabilities are often "frozen" at their open-circuit values, while E is regarded as constant; but because of the ambiguities that arise as a result of the nonlinearity of the magnetic circuit, this method is to be avoided.

Another method is to extract B_1, the fundamental component of the airgap flux-density distribution around the stator bore, by Fourier analysis of the calculated distribution: see Fig. 5. From B_1 the fundamental airgap flux/pole can be calculated, and then the peak flux-linkage per phase is given by (7), where D is the stator bore diameter, L_{stk} the stack length, k_{w1} the fundamental winding factor, and T_{ph} the number of turns in series per phase:

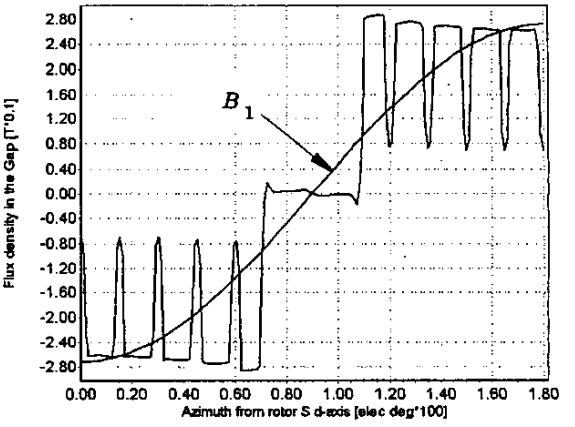

Fig. 5. Finite-element calculation of open-circuit flux-density around the airgap, over two half-poles. The fundamental component B_1 is also shown.

$$\Psi_1 = \frac{B_1 D L_{stk}}{p} \times k_{w1} T_{ph} \quad \text{V-s.} \tag{7}$$

The rms voltage induced in the phase winding by this flux-linkage is

$$V = \frac{\omega \Psi_1}{\sqrt{2}}. \tag{8}$$

If Ψ_1 is calculated for the open-circuit condition, this equation gives E, while (7) gives Ψ_{1Md}, the open-circuit flux-linkage due to the magnet. Under load, it gives the phase voltage V shown in Fig. 2.

When the fundamental distribution $B_1(\theta)$ is obtained, its phase angle can be used as a measure of δ (see Fig. 2), so that if E is assumed constant the reactances X_d and X_q can be extracted by setting $R_a = 0$ and using (4) with

$$\Psi_d = \Psi_1 \cos\delta = \Psi_{1Md} + \frac{L_d}{\omega} I_d$$
$$\text{and } \Psi_q = \Psi_1 \sin\delta = \frac{L_q}{\omega} I_q. \tag{9}$$

The values of $X_d = \omega L_d$ and $X_q = \omega L_q$ obtained in this way from the airgap B distribution do not include the slot-leakage reactance or the end-turn leakage reactance. The only simple way to add these elements is by estimating them with classical design formulas, [1].

III. Measuring the Flux-MMF Diagram

The flux-MMF diagram is measured during normal load-test conditions on a dynamometer as shown in Figs. 6 and 7.

The phase terminal voltage v and current i are recorded digitally and the flux-linkage waveform is obtained from the integral

$$\psi = \int (v - Ri)\,dt, \qquad (10)$$

where R is the phase resistance.

The test motor analyzed in this paper is a 230-V, 50-Hz, 2-pole single-phase capacitor motor with main and auxiliary phases whose winding axes are displaced by 90°. Both windings have 5 concentric coils per pole with approximately sinusoidal distribution of turns; see Fig. 8.

Dynamometer load tests are conducted with approximately sinusoidal currents supplied by a two-phase DSP-controlled PWM inverter. The amplitudes of the main and auxiliary phase currents are controlled to be in the inverse ratio of the effective turns in each winding, so that operation is balanced. The phase orientation of the current is also controlled by the inverter, using shaft position feedback from an optical encoder.

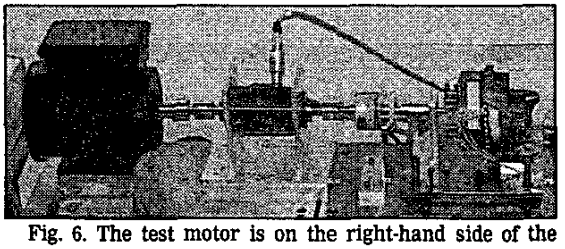

Fig. 6. The test motor is on the right-hand side of the picture, with an in-line torque transducer in the center and a brake machine on the left. Rotor position is measured by an in-line optical encoder.

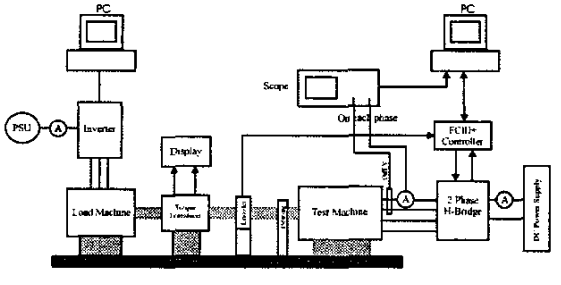

Fig. 7. Dynamometer and test configuration

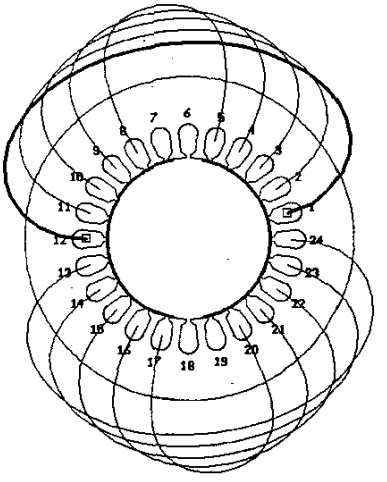

Fig. 8. Main phase winding of test motor.

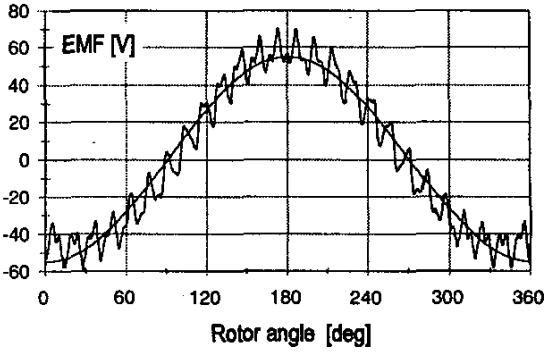

Fig. 9. Measured open-circuit EMF waveform of main phase winding at 1000 rpm. Magnet temperature = 25°C.

The measured open-circuit EMF waveform of the main phase at 1,000 rpm is shown in Fig. 9, together with its fundamental component, $E = 38.9$ V rms.

The test motor has no skew, so the EMF shows considerable ripple arising from the slotting on both the rotor and the stator. The open-circuit flux distribution in the airgap is far from sinusoidal, as shown by the finite-element calculation in Fig. 5.

It is very important to measure or estimate the magnet temperature at every test point, so that the correct remanent flux-density can be used in calculations. The same is true of the winding temperature, so that the phase resistances can be correctly calculated.

IV. Test Results

A. Measured Flux-MMF Diagram

Fig. 10 shows the flux-MMF diagram at a typical test point, with a sinusoidal current of 2.0 A (peak) at an angle $\gamma = +40°$ meaning that the current phasor leads the EMF phasor by 40°.

The torque calculated by (5) from the loop areas in Fig. 10 is 1.30 Nm. This includes the contributions from both the main and auxiliary phases, which are almost equal. Also shown is the i-ψ loop computed by the finite-element method without end-turn leakage correction. Without this correction the measured and calculated loops differ slightly, and further deviations arise from the PWM harmonics in the measured loops. However, the loop areas are remarkably close.

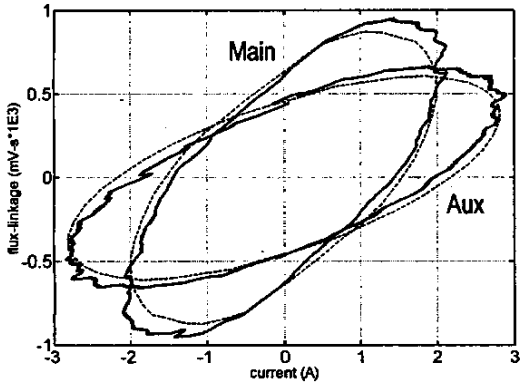

Fig. 10. Measured i-ψ loops for the main and auxiliary phase windings. The dotted lines show the loops derived from the finite-element method driven by the fundamental component of current.

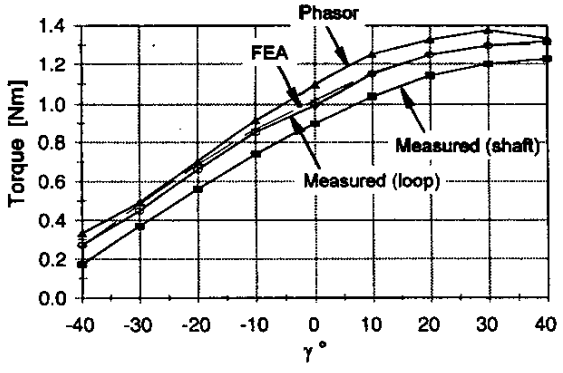

Fig. 11. Torque vs. γ obtained by measurement and calculation. Sinusoidal current, peak value 2.0 A.

Fig. 11 shows the torque vs. γ over a range from -40° to +40°, with constant current of 2 A peak at 1000 rpm. This current is close to the safe maximum of the motor. Close agreement is obtained between torque values from the i-ψ loops obtained by direct measurement and finite-element calculation, over the whole range. The shaft torque is about 0.1 Nm less than the loop torque, probably owing to a combination of friction and windage and a drag torque caused by iron loss.

Fig. 11 also shows the torque calculated by (1) after adjusting X_d and X_q to match the i-ψ loop obtained by the finite-element method at $\gamma = 40°$ and 2 A, with E = 38.9 V rms, the test value. At other values of γ the "phasor" method deviates because of variations in X_d and X_q caused by saturation.

B. Variation of X_d and X_q

Fig. 11 gives little information about the variation of X_d and X_q with current. Accordingly two series of finite-element calculations were carried out, one with current only in the d-axis and the other with current only in the q-axis. For each solution, X_d and X_q were obtained using (7-9). The result is given in Fig. 12, which expresses X_d as a function of I_d with $I_q = 0$, and X_q as a function of I_q with $I_d = 0$. In all cases it is assumed that E is constant, as in [8].

Fig. 12 shows a huge variation of 6:1 in X_q and almost 2:1 in X_d.

Calculations with current flowing simultaneously in both axes show that X_d is affected by I_q, being increased when $I_d < 0$ and decreased when $I_d > 0$, with $I_q > 0$. An example is shown in Fig. 13 which is computed for I_q = 2.0 A (peak), and varying I_d.

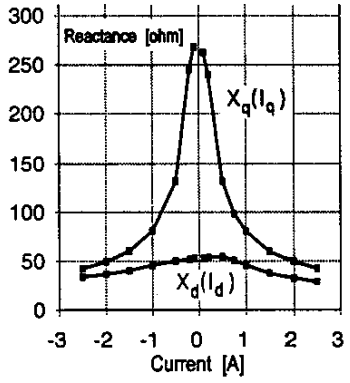

Fig. 12. Variation of X_d vs. I_d with $I_q = 0$, and of X_q vs. I_q with $I_d = 0$, calculated using (7-9) from finite-element data with constant E.

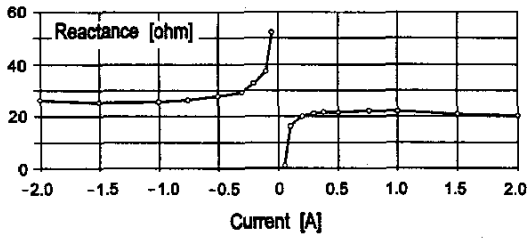

Fig. 13. X_d vs. I_d with I_q = 2.0 A (peak).

The discontinuity at $I_d = 0$ was mentioned earlier in connection with the "frozen permeability" method. It can be attributed to an error or variation ΔE from the open-circuit value E_0:

$$X_d = \frac{V_q - (E_0 + \Delta E)}{I_d} = \frac{V_q - E_0}{I_d} - \frac{\Delta E}{I_d}. \quad (11)$$

If E is assumed constant and equal to E_0, the value of X_d that will be inferred by using only the first term of (11) is in error by $\Delta E/I_d$, which is indefinite when $I_d = 0$.[a] Evidently the effect of cross-saturation is that E depends on the current components I_d and I_q as do X_d and X_q.

V. Conclusion

Experimental validation of the flux-MMF diagram for torque calculation has been given in the form of measured energy conversion loops and shaft torque measurements. The flux-MMF diagram is convenient to calculate by the finite-element method, and if the current waveform is known *a priori*, the terminal voltage can be calculated from $Ri + d\psi/dt$ directly, providing valuable information for drive design.

In contrast, the classical phasor-diagram method is only as accurate as the values of E, X_d and X_q at every load point. X_d and especially X_q vary widely as a function of current, and cross-saturation effects complicate these functions: for example, if E is assumed constant the variation of X_d with I_d can be discontinuous around $I_d = 0$. Since there is no practical means of calculating X_d and X_q accurately other than the finite-element method, it is hard to escape the conclusion that the classical method has little more than symbolic value and that the finite-element method should be used routinely instead. The phasor diagram is still useful as a guide, but inadequate as a model.

Although the finite-element method can be used to calculate E, X_d and X_q for use in the phasor diagram, this method applies only to motors that have sine-distributed windings and sinusoidal waveforms of EMF, current, and terminal voltage. The flux-MMF diagram method, on the other hand, is completely general and applies to motors that do not have these ideal properties.

VI. References

1. Hendershot JR and Miller TJE [1994] *Design of brushless permanent-magnet motors*, Magna Physics Publishing.

2. Miller TJE [1989] *Brushless permanent-magnet and reluctance motor drives.* Oxford University Press.

3. Jahns TM [1987] *Flux-weakening regime operation of an interior permanent-magnet synchronous motor drive*, IEEE Trans. **IA-23**, No. 4, July/August 1987, pp. 681-689.

4. Bianchi N and Bolognani S [1998] *Unified approach to the analysis and design of an AC motor drive for flux-weakening operation*, Conf. Rec. IEEE Industry Applications Society 33rd Annual Meeting, St. Louis, MO, USA, 12-15 October 1998, pp. 95-102.

5. Bianchi N and Bolognani S [1998] *Magnetic models of saturated interior permanent magnet motors based on finite-element analysis*, Conf. Rec. IEEE Industry Applications Society 33rd Annual Meeting, St. Louis, MO, USA, 12-15 October 1998, pp. 27-34.

6. Honda Y., Higaki T., Morimoto S. and Takeda Y [1998] *Rotor design optimisation of a multi-layer interior permanent-magnet synchronous motor*, IEE Proceedings, Electric Power Applications, **145**, No. 2, March 1998, pp. 119-124.

7. Nee H.-P., Lefevre L, Thelin P, Soulard J. [2000] *Determination of d and q reactances of permanent-magnet synchronous motors without measurements of the rotor position*, IEEE Trans. Industry Applications, **IA-36**, No. 5 , September/October 2000, pp. 1330-1335.

8. Popescu M, Miller TJE, McGilp MI, Strappazzon G, Trivillin N, Santarossa R [2002] *Line Start Permanent Magnet Motor: Single Phase Starting Performance Analysis*, Conf. Rec. IEEE Industry Applications Society, 37th Annual Meeting, Pittsburgh, USA, 13-18 October 2002, pp. 2499-2506.

9. Miller TJE [1981] *Methods for testing permanent-magnet AC motors.* IEEE Industry Applications Society Annual Meeting (IAS), Toronto, October 1981, pp. 494-499.

10. Ionel DM, Eastham JF, Miller TJE and Demeter E. [1998] *Design Considerations for permanent magnet synchronous motors for flux weakening applications*, IEE Proceedings, Electr. Power Appl., Vol. 145, No.5, September 1998, pp. 435-440.

11. Staton DA, Soong, WL, Deodhar RP and Miller TJE [1995] Torque prediction using the flux-MMF diagram in AC, DC and reluctance motors, IEEE Transactions Industry Applications, Vol.32, No.1, Jan-Feb. 1996, pp. 180-188.

12. Soong WL, Staton DA and Miller TJE [1994] *Design of a new axially-laminated interior permanent-magnet motor.* IEEE Trans., Vol.31, No.2, March/April 1995, pp.358-367.

[a] This explanation was originally suggested to one of the authors by R.J. Krefta.